J Mater Sci: Mater Electron (2022) 33:24559–24570

Band gap tailoring and photosensitivity study of Al-doped SnO_2 nanocrystallites prepared by sol–gel technique

Binod Bihari Panda[1,*], Debakanta Tripathy[1], and Niladri Maity[1,*]

[1] *Department of Chemistry, Indira Gandhi Institute of Technology, Sarang, Dhenkanal, Odisha 759146, India*

Received: 2 March 2022
Accepted: 18 September 2022
Published online: 30 September 2022

ABSTRACT

Electrical, optical and photosensitivity of aluminium-doped tin oxide (Al-SnO_2) nanocrystallites prepared by sol–gel technique and annealed at 400 °C and 500 °C are studied. The synthesized nanocrystallites are characterized using spectroscopic techniques such as powder X-ray diffraction (PXRD), scanning electron microscopy (SEM), Fourier transform infrared (FTIR) spectroscopy, energy-dispersive X-ray spectroscopy (EDX) and UV–VIS-DRS spectroscopy. The PXRD data confirm the development of polycrystalline nanocrystallites having crystal size ≈ 6.8 nm at 400 °C which increases to ≈ 8.7 nm on annealing at 500 °C. SEM images illustrate the formation of nanoclusters. Broad characteristics bands of FTIR spectra demonstrate the presence of physical interaction between SnO_2 and Al_2O_3. EDX spectra illustrate the presence of aluminium, tin and oxygen in the particles annealed at 400 °C and 500 °C with composition $Sn_{0.726}Al_{0.274}O_2$ and $Sn_{0.809}Al_{0.191}O_2$, respectively. UV–VIS-DRS spectroscopy illustrates that the band gap energy of 400 °C and 500 °C annealed materials are 3.42 and 3.35 eV, respectively. First time, the electrical properties and photosensitivity of the Al-SnO_2 nanocrystallites annealed at two different temperatures are studied by making the particles into thin films of thickness 103μ (400 °C) and 106μ (500 °C) on glass substrate.

1 Introduction

Nowadays metal oxide nanocrystallites are creating immense interest among researchers because of their unique characteristics, wide range of applications and stability. They are key materials for optoelectronic devices [1–5]. Among the oxides, SnO_2 is a significant n-type semiconducting material and is useful in fabrication of solid-state gas sensors [6], transparent conducting electrodes [7], rechargeable Li-batteries [8] optical and electronic devices [9], catalyst for photo-degradation & organic conversion [10], photo-electrodes of photovoltaic cells for solar energy conversion and antistatic coating [11–14]. Researchers have reported that the optoelectronics

Address correspondence to E-mail: binodgcek@gmail.com; niladriiitb@gail.com

https://doi.org/10.1007/s10854-022-09167-9

properties of SnO_2 can be tailored by doping aluminium in SnO_2 crystals for making efficient sensor, active anode, display devices, vacuum electronics and catalysts [15–18]. So far, as the properties and specific application is concern, the synthesis technique of nanocrystallites plays a vital role. The diverse methods used for the synthesis of Al-SnO_2 nanocrystallites of varying structure and morphology are co-precipitation method [19], chemical vapour deposition (CVD), vapour–liquid–solid approach (VLSA), rapid thermal evaporation (RTE) and the sol–gel method [20–25]. The ion implantation method can also be used for preparing mixed metal oxides [26]. Among these techniques, the sol–gel method has established its credibility as it is a simple, reproducible and inexpensive path for the production of nanocrystallites. Preparation of multi-component oxides applying this strategy is appropriate as it has the competence to bring several components into the solution phase, size and morphology can be controlled, processing and sintering can be performed at low temperature, and better homogeneity and phase purity can be achieved [27].

At present, designing of optical materials of non-toxic elements is a growing field of research. In view of the above facts, herein an attempt is taken to prepare Al-doped SnO_2 nanocrystallites by the sol–gel technique. The synthesized materials are characterized using PXRD, SEM and EDX. The optical properties are studied by using the UV–VIS-DRS spectroscopic technique and electrical and photosensing application by current–voltage (I–V) measurement.

2 Experimental details

2.1 Chemicals

Chemicals like stannous chloride (98%), aluminium sulphate (98%), n-hexane (95%), ethanol (95.5%), acetone (99.5%), methanol (99.9%) and aqueous ammonia (25%) were purchased from Merck India Ltd and were used for preparation of nanocrystallites without further purification. Double distilled water was used throughout the experiments for the preparation of solutions.

2.2 Synthesis of nanocrystallites and thin films

Al-doped SnO_2 nanocrystallites were prepared by the sol–gel method. First 100 ml of aqueous-ethanol solution (1:1) of aluminium sulphate (Al_2SO_4) (2 mmol) and 100 ml of aqueous-ethanol solution (1:1) of tin dichloride dihydrate ($SnCl_2{\cdot}2H_2O$) (14 mmol) were prepared. Then both the solutions were mixed under vigorous stirring, to get transparent sol. Thereafter, ammonia solution was poured drop by drop into the solution with constant stirring in magnetic stirrer to get gel. The gel was filtered, washed with methanol and then dried at 200 °C for 1 h to get dried sample. The dried sample was further annealed at 400 °C and 500 °C for 2 h to achieve a fine homogeneous powder of Al-SnO_2 nanocrystallites.

A part of the annealed nanopowder was dispersed in the organic solvent [28], and thin films of the nanocrystallites were prepared on glass substrate by the spin coating technique at the rpm rate of 2000 for the 40 s at room temperature. The thicknesses of the prepared thin films were measured gravimetrically using the relation 1 [29].

$$t = \frac{w}{Ad} \tag{1}$$

where t = thickness of the deposited film, W = weight of the film, A = total surface area of the film, and d = density of the film with the assumption that the film density is same as the bulk density. The measured thicknesses of the films were found to be 103 and 106μ for 400 °C and 500 °C annealed nanocrystallites.

2.3 Characterization

The phases, crystallinity and structural analysis of Al-doped SnO_2nanocrystallites were studied by powder X-ray diffraction (PXRD) carried out by Siemens (Cheshire, UK) D 5000 X-ray diffractometer equipped with CuKα radiation source (λ = 1.5406 Å) at 45 kV and 40 mA with a standard monochromator equipped with a Ni filter, in the range of 10–80°, using the step size 0:013° and time step 13.6 s. The scanning electron microscopy (SEM) images were recorded in a Hitachi S-3000 N scanning electron microscope operated at 10 kV to investigate the surface morphology. EDX was carried out in Zeiss

EDAX EVO-18 at 15 k Volt. FTIR spectra were recorded at 4000–400 cm^{-1} on a Bruker Alpha spectrometer equipped with a DTGS KBr detector. UV–VIS-DRS spectra were recorded in UV–VIS-DRS spectrophotometer Cary 5000 by diluting the samples with KBr. The current–voltage (I–V) of the thin films was also measured in dark and light using 100 W tungsten bulb to study photosensitivity.

3 Results and discussion

3.1 PXRD structural analysis

The powder X-ray diffraction (PXRD) patterns of the annealed samples of Al-doped SnO_2 nanocrystallites are shown in Fig. 1. All peaks observed in the patterns can be indexed for SnO_2 of space group $P4_2/mnm$ with tetragonal structure (reference to ICDD card no. 41-1445) [27].

The diffraction patterns attribute the formation of polycrystalline nanocrystallites with peaks along (110), (101), (200), (211), (220), (116), (002), (202) and (310) planes. Sharpening of Bragg's reflections on increasing the annealing temperature from 400 to 500 °C of the sample shows that growth of crystals is taking place (Fig. 1) along (110), (101) and (211) planes [30] with creation of new nucleating centres in the whole lattice [31]. The non-appearance of peak for aluminium in the PXRD pattern attributes the integration of aluminium atoms homogeneously into the SnO_2 crystal lattice. Rather a slight shifting of (110), (101), (200), (211) and (220) peaks is observed towards higher angle (26.70 °C, 33.92 °C, 38.01 °C, 51.92 °C and 54.66 °C, respectively) for Al-SnO_2 nanocrystallites (annealed at 400 °C) from the pure SnO_2 (26.69 °C, 33.88 °C, 37.95 °C, 51.79 °C and 54.62 °C, respectively) [32]. Similar type of shifting is also cited earlier by Yahia and co-workers where they have reported the shifting of XRD pattern to higher angle by incorporation of Ni ions in the crystal lattice of CdS [33]. The PXRD pattern of Al-SnO_2 is found to be shifting of peaks (110), (101), (200) and (211) further towards right (26.74 °C, 34.05 °C, 38.45 °C, 51.91 °C and 54.63 °C) with the increase in annealing temperature (500 °C), which attributes the minimization of defects level in the crystallites, imperfections and surface traps. It has also been reported that in the enhancement of annealing temperature, the defects level, imperfections and the surface traps of the film get minimized. So the XRD peaks shift towards higher angles [31]. From the PXRD data, the size of nanocrystallites and micro-strain are calculated using Sherrer's Eq. 2 and Williamson-Hall (W–H) analysis (Eq. 3) considering the intercept and slope of the plot of $4\varepsilon \sin\theta$ vs $\beta_{hkl}\cos\theta$ plots (Fig. 2A and B) [34]. Scattering of points in the plot may be due to low correlation coefficient (R^2 are 0.12 and 0.39 for 400 °C and 500 °C annealed Al-SnO_2 nanocrystallites) [35]. To compare the accuracy of the results, size-strain plot (SSP) and Halder-Wagner (H-W) method are employed. SSP is drawn taking ($d^2\beta\cos\Theta$) along X-axis and ($d\beta\cos\Theta)^2$ along Y-axis of Eq. 4. Considering the slope and intercept of plot (SF-1), size and micro-strain are calculated. Similarly size and micro-strain of nanocrystallites are measured by H-W method from the slope and intercept of the plot drawn taking $(\beta\cos\Theta/\lambda)/[2d\sin\Theta/\lambda]^2$ along X-axis and $[(\beta\cos\Theta/\lambda)/(2d\sin\Theta/\lambda)]^2$ along Y-axis (SF-2) of Eq. 5 [36] which are reported in Table 1. The results illustrate that the average size measured are analogous. Herein the negative slope of the plots (Fig. 2A and B) indicates the presence of micro-strain in the synthesized samples [34]. The values of decreasing micro-strain with the increase in annealing temperature implies the sample is mechanically fit to resist different kinds of deforming forces. It reduces the chances of crystal misalignment and internal lattice deformation. Accounting the intense peaks (101 and 211) of PXRD pattern, the d-spacing and $\Delta(2\theta)$ are reported in Table-ST-I and dislocation density (δ), stacking faults (Fs) and lattice parameters (a and c) are calculated using Eqs. 6–8 [31, 37].

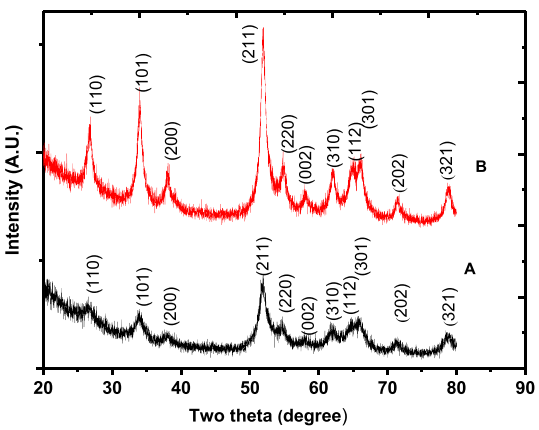

Fig. 1 PXRD pattern of Al-SnO_2 nanocrystallites annealed at **A** 400 °C and **B** 500 °C

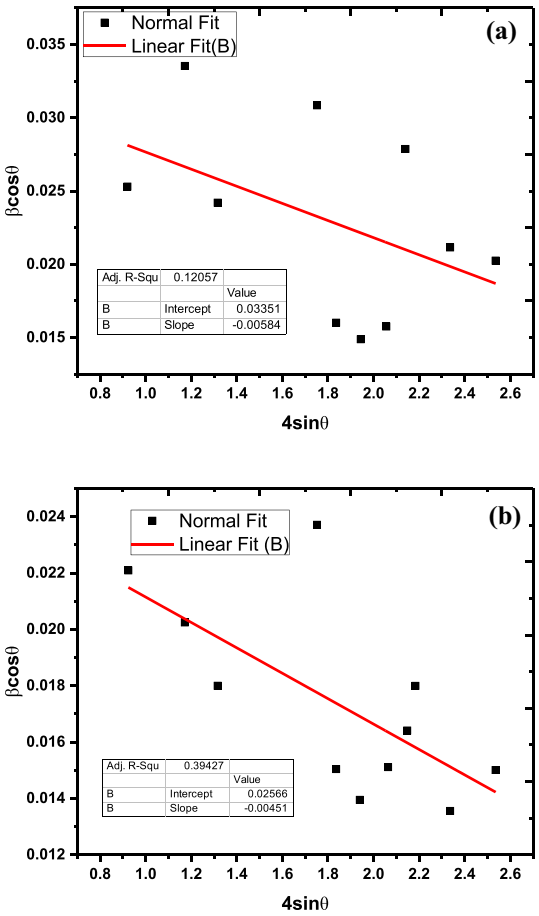

Fig. 2 **A** Williamson–Hall plot for the Al-SnO_2 nanocrystallites annealed at 400 °C. **B** Williamson–Hall plot for the Al-SnO_2 nanocrystallites annealed at 500 °C

$$D = \frac{k\lambda}{\beta_{hkl}\cos\theta} \tag{2}$$

$$\beta_{hkl}\cos\theta = \left(\frac{k\lambda}{D}\right) + 4\varepsilon\sin\theta \tag{3}$$

$$(d\beta\cos\theta)^2 = \frac{k\lambda}{D}d^2(\beta\cos\theta) + \frac{\varepsilon^2}{4} \tag{4}$$

$$\left(\frac{(\beta\cos\theta/\lambda)}{(2d\sin\theta/\lambda)}\right)^2 = \frac{(\beta\cos\theta/\lambda)}{(2d\sin\theta/\lambda)^2} \times \frac{1}{D} + \left(\frac{\varepsilon}{2}\right)^2 \tag{5}$$

$$\delta = \frac{1}{D^2} \tag{6}$$

$$F_S = \frac{2\pi^2 \times \Delta(2\theta)}{45 \times \sqrt{3} \times \tan\theta} \tag{7}$$

$$\frac{1}{d^2} = \frac{h^2 + k^2}{a^2} + \frac{l^2}{c^2} \tag{8}$$

where D = is the size of crystallites, k is 0.94, λ is the X-ray wavelength (1.54060 Å), β is the full width at half maximum in radians, δ is dislocation density,ε is micro-strain, and θ is Bragg's angle.

The calculated parameters of the samples are reported in Table 1 with units [38, 39]. The data show the decreasing of d-spacing. The decreasing of d-spacing and smaller radius of aluminium (Al^{3+} = 0.64 Å and Sn^{4+} = 0.71 Å) attribute the successful incorporation of aluminium in the SnO_2 crystal lattice. The lattice parameters calculated for Al-SnO_2 (a = 2.403 Å, c = 1.686 Å) are lower than the pure SnO_2 (a = 4.7 Å, c = 3.2 Å)[40], also proving the successful replacement of Sn ions by Al ions. Similarly on annealing further, a small decrease in lattice parameters is observed which may be due to development of oxygen vacancies in the crystal lattice [41, 42]. The increase in annealing temperature may be the reason of enhancement of crystal size and tetragonality (Table 1).

The other parameter like dislocation density of Al-SnO_2 nanocrystallites annealed at 400 °C is found to be 4.68 × 10^{-2} which is increasing on annealing the sample at 500 °C. This shows that there may be the possibility of gradual improvement in crystalline quality and reduction in all kinds of defects or dislocation. Hassan et al. have also reported that all kind of defects are decreasing with the increase in crystal quality by decreasing of dislocation density [43]. The decreasing of Fs on annealing (Table 1) proves the increasing of crystal quality and reduction in planar misalignments.

3.2 SEM analysis

The surface morphology of the synthesized and annealed samples has been studied by a scanning electron microscope, and the micrographs in the magnification of 25KX and 50KX are shown in Fig. 3. Figure 3A and B shows the micrographs of Al-doped SnO_2 sample annealed at 400 °C, and C and D show the micrographs of the sample annealed at 500 °C.

All the SEM images of the samples show agglomeration of nanocrystallites to form nanoclusters. The size of nanoclusters calculated for the Al-SnO_2 nanocrystallites from SEM images of sample annealed at 400 °C and 500 °C is found to be ≈ 60 and ≈ 100 nm [44].

Table 1 Structural parameters nubmeralised from PXRD pattern of Al-doped SnO_2 nanocrystallites prepared by sol–gel method and annealed at 400 °C and 500 °C

Sample	Annealing Temp	d-spacing (Å)	a (Å)	c (Å)	Scherrer's Method Size D (nm)	W–H Method		S–S-P Method		H-W Method		Tetragonality	F_5
						Size D (nm)	Strain (ε)	Size D (nm)	Strain (ε)	Size D (nm)	Strain (ε)		
$Sn_{0.726}Al_{0.274}O_2$	400 °C	0.978	2.403	1.686	4.62	4.20	5.8×10^{-3}	4.99	3.4×10^{-3}	3.17	3.0×10^{-1}	0.7016	0.595
$Sn_{0.809}Al_{0.191}O_2$	500 °C	0.966	2.390	1.684	6.16	5.79	4.5×10^{-3}	6.03	3.3×10^{-3}	4.10	2.4×10^{-1}	0.7046	0.592

3.3 Elemental analysis

EDX spectroscopy study is performed to know the chemical composition of prepared Al-SnO_2 annealed at 400 °C and 500 °C and is shown in Fig. 4A and B. The EDX reveals the presence of tin, aluminium and oxygen in the synthesized samples. A sharp peak for Sn and weaker peaks for O and Al are observed in Fig. 4A. In Fig. 4B, reduction in peak intensity for 'O' is observed. It proves that more oxygen deficiency is taking place on annealing which may lead to turn the nanocrystallites showing better n-type semiconducting properties [45].

These results may be due to de-absorption of oxygen and release of trapped electrons on annealing the samples. However, the composition (empirical formula) calculated from the EDX data is found to be $Sn_{0.726}Al_{0.274}O_2$ (annealed at 400 °C) and $Sn_{0.809}Al_{0.191}O_2$ (annealed at 500 °C) which are closer to the expected experimental ratio of Sn:Al (1:0.28). The small difference of expected experimental ratio and ratio obtained from EDX data may be due to error in weighting of chemicals and experimentation. Thus the Al-doped SnO_2 nanocrystallites might have application in optoelectronic devices [44].

3.4 FTIR analysis

Figure 5A and B shows FTIR transmittance spectra of Al-doped SnO_2 nanocrystallites annealed at 400 °C and 500 °C, respectively. The transmittance spectra of Fig. 5A illustrates peaks at 3389.54, 2487.84, 1636.29, 1103.02, 923.51 and 615.39 cm^{-1} but peaks at 3412.97, 2925.80, 1636.61, 1103.42, and 624.32 cm^{-1} are observed in Fig. 5B.

The peaks at 3389.54 and 3412.97 cm^{-1} are related to the O–H bond stretching vibration of water molecules [46]. The transmittance peaks in position 2487.84 and 2925.80 cm^{-1} may be due to vibration carbon dioxide. This shows that the samples might have absorbed moisture and carbon dioxide molecules from the atmosphere [47, 48]. The peaks at 1636.29 and 1636.61 $cm^{-1}$are related to flexural vibrations groups of O–H and in water molecules and Sn-OH bonds [11, 49]. The peaks at 1103.02 and 1103.42 cm^{-1} are due to the presence of inorganic ions [50]. Broad transmittance peak at 615.39 and 624.32 cm^{-1} can be attributed to of Sn–O-Al bond, whereas weak one at 923.51 cm^{-1} is related to Al-O bound [11, 49].

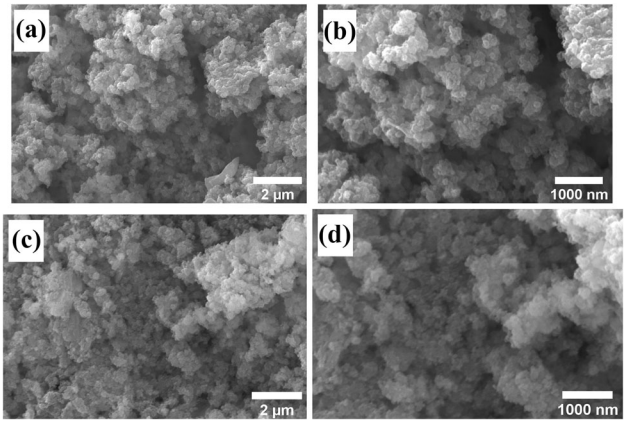

Fig. 3 Top view SEM image of sol–gel-synthesized Al-SnO_2 nanocrystallites annealed at 400 °C in the magnification of A-25KX and B-50KX and 500 °C in the magnification of C-25KX and D-50KX

3.5 Optical and photosensing properties

The UV–VIS diffuse absorption/reflectance spectroscopy in the wavelength range 200–800 nm is performed for the synthesized sample annealed at 400 °C and 500 °C to study the effect of oxygen vacancies on optical properties and electrical properties as the oxygen vacancy influences the electrical [51] and optical properties [52] of the Al-doped SnO_2 nanocrystallites. Figure 6 shows the absorbance spectra of nanocrystallites annealed at 400 °C and 500 °C in the visible range though the SnO_2 and Al_2O_3 are of high band gap.

This may be attributed to the defect and oxygen vacancies as shown by EDX data and the decrease in the lattice parameters [42, 53]. The absorption edge of nanocrystallites annealed at 400 °C and 500 °C is located in the visible region. So the synthesized nanocrystallites may be used as photosensing materials in visible light. The spectra also show the red shift of the absorption from 380 to 410 nm of nanocrystallites on annealing. The direct band gap of nanocrystallites annealed at 400 °C and 500 °C is estimated from tauc's plots taking hυ in X-axis and $(\alpha h\upsilon)^2$ in Y-axis of Eq. 8 and considering the points at which the extrapolated lines intercept the X-axis (Fig. 7) [54–56]. The 'n' of Eq. 9 is either 1/2 or 2/3 for direct transition, two or three for indirect transition according to allowed or forbidden, respectively. It is reported earlier that SnO_2 is a direct energy band gap n-type semiconductor metal oxide. Herein thus 'n' value is taken ½ and the band gap energies are measured and found to be ≈ 3.42 and ≈ 3.35 eV for 400 °C and 500 °C annealed samples, which attribute the red shift on annealing. A similar result has also been reported by Mendoza–Damián [19, 39].

$$\alpha h\nu = \alpha_0 (h\nu - E_g)^n \tag{9}$$

The observed band gap of the Al-doped SnO_2 nanocrystallites annealed at 500 °C is considerably smaller than that of the Al-doped SnO_2 nanocrystallites annealed at 400 °C which may be due to the presence of defects, increase in size from 4.62 to 6.16 nm and increase in oxygen vacancies as shown by EDX data and decrease in the lattice parameters [42].

The other properties, such as refractive index and dielectric constant, the electrical properties like sheet resistance and resistivity and photosensing properties such as photosensor efficiency (P), photosensitivity (S) and photorensposivity of the synthesized and annealed Al-doped SnO_2 nanocrystallites are also calculated from reflectance (Fig. 8), absorbance spectroscopy and current–voltage (I–V) measurement (Fig. 9) using Eqs. (10–17) [57–59] and are reflected in Table 2.

$$n = n^0 [1 + \alpha e^{-\beta E_g}] \tag{10}$$

where n = refractive index, n^0 = 1.73, α = 1.9017, β = 0.539 $(eV)^{-1}$ and E_g = band gap

$$\varepsilon_\infty = n^2 \tag{11}$$

$$\varepsilon_0 = 18.52 - 3.08 E_g \tag{12}$$

where ε_∞ = high frequency dielectric constant, ε_0 = static dielectric constant

$$R_{sheet} = 4.53 \frac{V}{I} \tag{13}$$

$$\rho = R_{sheet} \times t \tag{14}$$

where R_{sheet} = sheet resistance, V = voltage, I = current and t = thickness of film.

$$P = \frac{I_p}{I_d} \tag{15}$$

$$R = \frac{I_p - I_d}{AP_i} \tag{16}$$

$$S\% = \frac{R_d - R_l}{R_d} \times 100 \tag{17}$$

where P = photosensor efficiency, I_p = photonic current, I_d = dark current, R = photoresposivity,

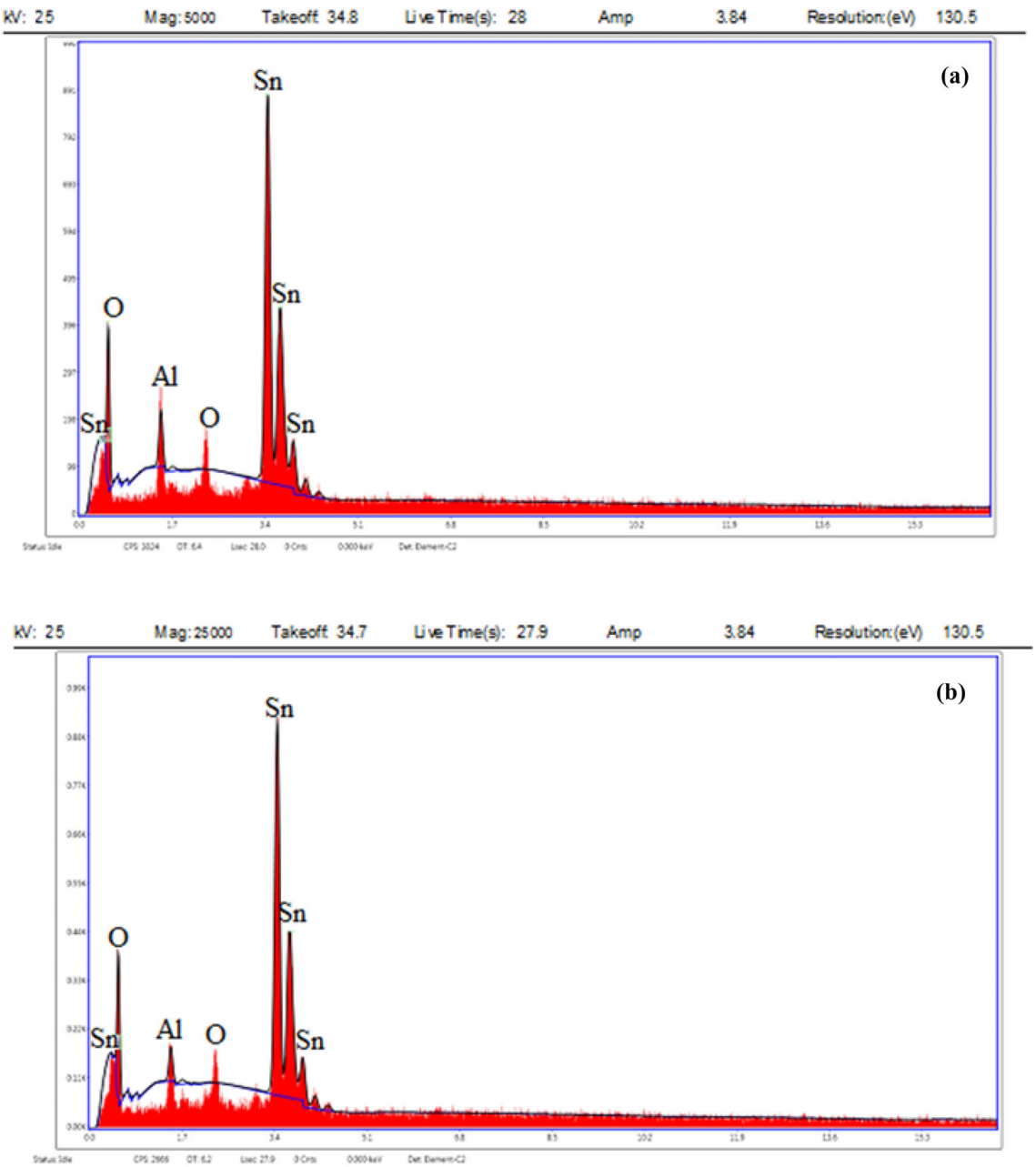

Fig. 4 **A** EDX of sol–gel-synthesized Al-SnO_2 nanocrystallites annealed at 400 °C. **B** EDX of sol–gel-synthesized Al-SnO_2 nanocrystallites annealed at 500 °C

A = effective film area, P_i = power of incident light, $S\%$ = photosensitivity, R_d = resistance in dark and R_l = resistance in light.

The refractive index is very much useful to study the behaviour of light passing through materials. It is an important parameter to study the optical and electrical properties of semiconducting materials. The velocity of light passing through a material decreases by increasing the refractive index [60]. Materials with a high refractive index can trap more incidents light [61]. The relative permittivity of a material is determined from its dielectric constant. It is a significant factor for characterization of capacitors. Materials with high dielectric constant are used in

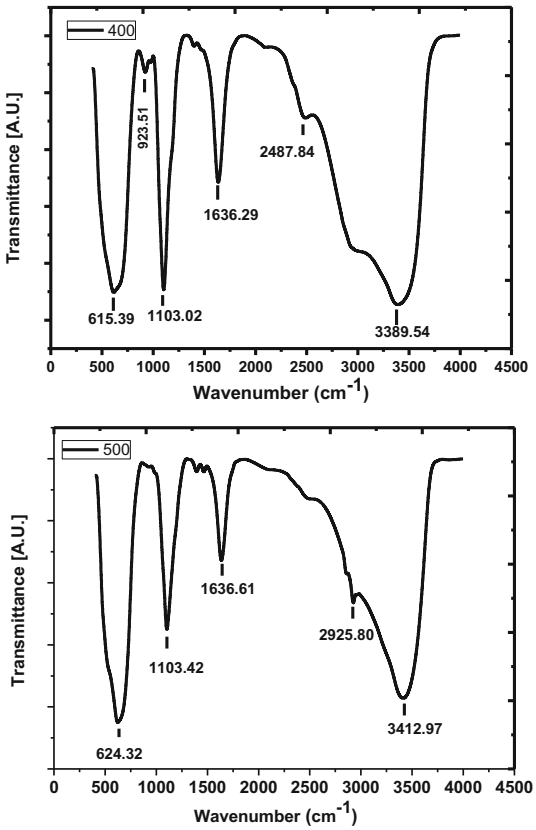

Fig. 5 **A** FTIR spectra of sol–gel-synthesized Al-SnO_2 nanocrystallites annealed at 400 °C. **B** FTIR spectra of sol–gel-synthesized Al-SnO_2 nanocrystallites annealed at 500 °C

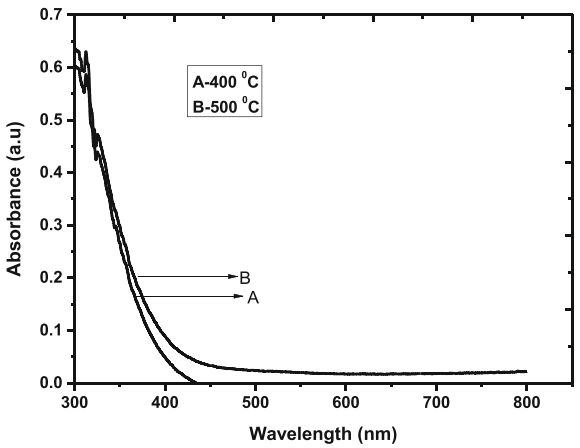

Fig. 6 UV–Vis spectra of sol–gel-synthesized Al-SnO_2 nanocrystallites annealed at **A** 400 °C and **B** 500 °C

semiconductor manufacturing processes, memory cell dielectrics, gate dielectrics and passive components. The measured values of the refractive index, dielectric constant, sheet resistance and resistivity calculated using the above-mentioned relations are

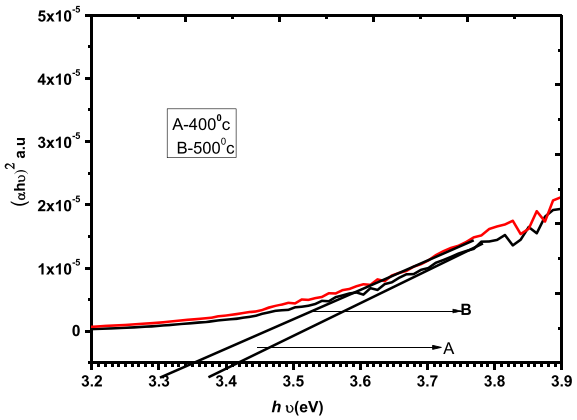

Fig. 7 Tauc's plot for band gap determination of Al-SnO_2 nanocrystallites annealed at **A** 400 °C and **B** 500 °C

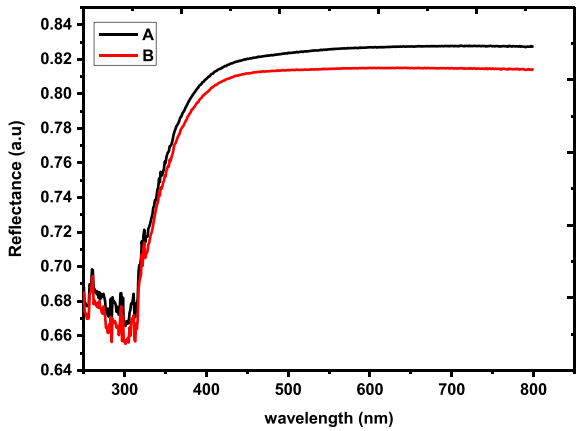

Fig. 8 Reflectance spectra of sol–gel-synthesized Al-SnO_2 nanocrystallites annealed at **A** 400 °C and **B** 500 °C

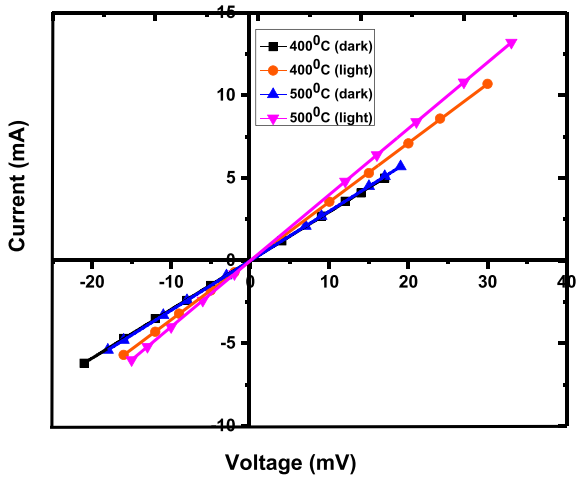

Fig. 9 I-V characteristics curve of sol–gel-synthesized Al-SnO_2 nanocrystallites annealed at **A** 400 °C and **B** 500 °C

Table 2 The optical electrical and photosensing parameter of Al-doped SnO_2 nanocrystallites prepared by sol–gel method and annealed at 400 °C and 500 °C

Optical properties	Band gap (eV)	Refractive index	ε_∞	ε_0	R_{sheet} Ω		$\rho \times 10^{-3} \Omega cm$		Photosensor efficiency (P)	Photosensitivity (S)	Photorensposivity
					Dark	Light	Dark	Light			
400 °C	3.42	4.7	24.01	8.51	15.35	12.72	4.6	3.6	1.17	14%	1.25×10^{-4}
500 °C	3.35	4.9	22.09	8.11	15.1	11.325	4.5	3.3	1.7	24%	2.5×10^{-3}

reported in Table 2. The results show that the synthesized Al-doped SnO_2 particles have significance in optical and electro-optical applications [62]. Here the data show the increase in refractive index and decrease in dielectric constants (both high-frequency dielectric constant and static dielectric constant) (Table 2) on annealing at 500 °C supporting its importance in semiconductor industries. The photosensing properties of the thin films synthesized from the nanocrystallites annealed at 400 °C and 500 °C are studied in dark and light of using 100 W tungsten bulb by measuring the change of current vs voltage. The I–V plots passing through the origin show the ohmic nature of films (Fig. 9). The radical increase in photocurrent on the illumination of light is attributed to the creation of electron–hole pair in conduction and valence bands by incident photons. The photon energy may be the cause of breaking the covalent bond to increase the free hole and electron in valence and conduction band. The sheet resistance (R_{sheet}) and resistivity (ρ) of the thin films, measured from the I-V plots, are reported in Table 2. The results show the decrease in R_{sheet} and ρ on annealing. The photosensing properties of the synthesized materials have also been studied from the I–V curves and are reported in Table 2.

Results show that the properties improve on annealing. The photosensitivity of Al-SnO_2 annealed at 500 °C is found to be 24% which is higher than the photosensitivity of CdSe (12%) reported by Mahato et al. [63] and SnO_2 (18%) annealed at 400 °C reported by Badr Aly [64] The schematic representation of photosensitivity mechanism of sol–gel-synthesized Al-doped SnO_2 thin film under the illumination of light is shown in Fig. 10.

4 Conclusions

The Al-doped SnO_2 nanocrystallites are synthesized by the sol–gel technique, and annealing effect is studied at two different temperatures. The results show that, in the SnO_2 crystal lattice, aluminium is incorporated forming interstitially or substitutionally solid solution which on annealing creates oxygen deficiency in the crystal lattice. SEM micrograms show that the synthesized materials are composed of nanoclusters with the foam-like structure which is suitable for application as photosenser. The shifting and widening of FTIR peaks illustrate the physical

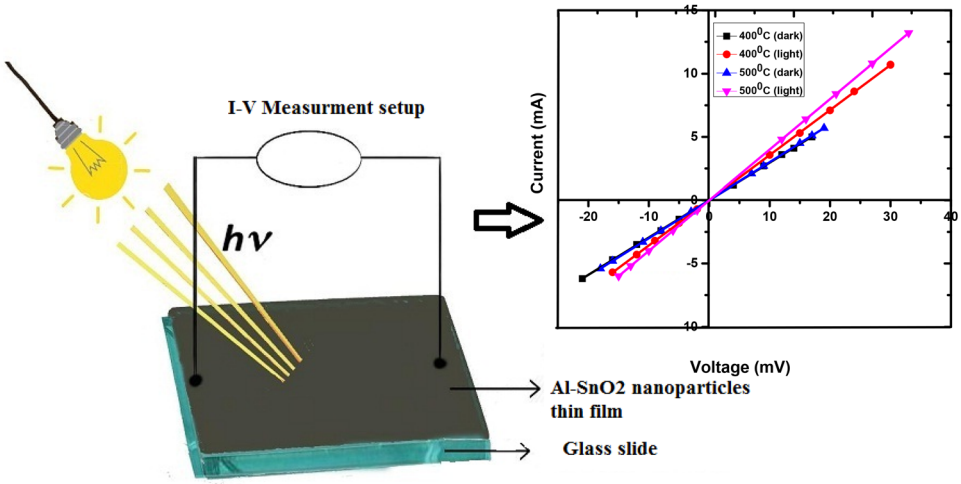

Fig. 10 Schematic representation of photosensitivity mechanism of sol–gel-synthesized Al-SnO_2 nanocrystallites thin film under illumination of light

interaction of SnO_2-Al_2O_3 nanocrystallites. The decrease in dislocation density, micro-strain and increase in crystalline quality, n-type direct band gap semiconducting character and resistivity data prove that Al-doped SnO_2 nanocrystallites are useful materials for fabrication of optoelectronic devices.

Author contributions

All authors contributed to the study conception and design. Material preparation, data collection and analysis were performed by BBP (binodgcek@gmail.com), DT (dtripathy579@gmail.com) and NM (niladriiitb@gail.com). The first draft of the manuscript was written by BBP, and all authors commented on previous versions of the manuscript. All authors read and approved the final manuscript.

Funding

The authors declare that no funds, grants, or other support were received to carry out the work or during the preparation of this manuscript.

Data availability

Data sharing not applicable to this article as no datasets were generated or analysed during the current study.

Declarations

Conflict of interest The authors have no relevant financial or non-financial interests to disclose. The corresponding author states that there is no conflict of interest on behalf of all authors.

Ethical approval Not applicable.

Consent to participate All authors participate in this work.

Consent to publish All authors agree to publish this work.

Supplementary Information: The online version contains supplementary material available at https://doi.org/10.1007/s10854-022-09167-9.

References

1. T. Coutts, D. Young, X. Li, MRS Bull. **25**, 58 (2000)
2. C. Granqvist, Sol. Energy Mater. Sol. Cells **91**, 1529 (2007)
3. Q. He, Y. Ni, S. Ye, RSC Adv. **7**, 27089 (2017)
4. L. Fan, Y. Li, X. Lin, J. Peng, G. Ju, S. Zhang, L. Chen, F. He, Y. Hu, RSC Adv. **7**, 44908 (2017)
5. V.V. Kutwade, K.P. Gattu, A.S. Dive, M.E. Sonawane, D.A. Tonpe, R. Sharma, J. Mater. Sci. Mater. Electron. **32**, 6475 (2021)
6. S.H. Saeedabad, G.S. Selopal, S.M. Rozati, Y. Tavakoli, G. Sberveglieri, J. Electron. Mater. **47**, 5165 (2018)
7. J.H. Kim, T.W. Kang, S.N. Kwon, S.I. Na, Y.Z. Yoo, H.S. Im, T.Y. Seong, J. Electron. Mater. **46**, 306 (2017)
8. Z. Peng, Z. Shi, M. Liu, Chem. Commun. **21**, 2125 (2000)

9. M. Yehia, S. Labib, S.M. Ismail, J. Electron. Mater. **48**, 4170 (2019)
10. S. Chen, Z. Sun, L. Zhang, H. Xie, Catalysts **10**, 117 (2020)
11. R. Niranjan, Y. Hwang, D. Kim, S. Jhung, J. Chang, I. Mulla, Mater. Chem. Phys. **92**, 384 (2005)
12. G. Guzman, B. Dahmani, J. Pütz, M. Aegerter, Thin Solid Films **502**, 281 (2006)
13. M. Abrari, M. Ghanaatshoar, H.R. Moazami, S. Saeed, H. Davarani, J. Electron. Mater. **48**, 445 (2019)
14. S. Asaithambi, P. Sakthivel, M. Karuppaiah, R. Murugan, R. Yuvakkumar, G. Ravi, J. Electron. Mater. **48**, 2183 (2019)
15. R. Alcantara, F.J. Fernandez-Madrigal, C. Perez-Vicente, J.L. Tirado, J.C. Jumas, J. Olivier-Fourcade, Chem. Mater. **12**, 3044 (2000)
16. M. Saha, A. Banerjee, A. Halder, J. Mondal, A.A. Sen, H.S. Maiti, Sens. Actuat. B Chem. **79**, 192 (2001)
17. L. Ma, Y. Ye, L. Hu, K. Zheng, T. Guo, Phys. E Low-Dimensional Syst. Nanostruct. **40**, 3127 (2008)
18. A. Ballarini, C. Ricci, S. de Miguel, O. Scelza, Catal. Today **133–135**, 28 (2008)
19. F.J. Tzompantzi, R. Gomez, G. Mendoza-Damián, A. Hernández-Gordillo, F. Tzompantzi, R. Gómez, J. Nanosci. Nanotechnol. **15**, 7258 (2015)
20. J.Q. Hu, X.L. Ma, N.G. Shang, Z.Y. Xie, N.B. Wong, C.S. Lee, S.T. Lee, J. Phys. Chem. B **106**, 3823 (2002)
21. F. Gu, S. Wang, C. Song, M. Lü, Y. Qi, G. Zhou, D. Xu, D. Yuan, Chem. Phys. Lett. **372**, 451 (2003)
22. D. Calestani, L. Lazzarini, G. Salviati, M. Zha, Cryst. Res. Technol. **40**, 937 (2005)
23. H.W. Kim, N.H. Kim, J.H. Myung, S.H. Shim, Phys. Status Solidi Appl. Mater. Sci. **202**, 1758 (2005)
24. H. He, T.H. Wu, C.L. Hsin, K.M. Li, L.J. Chen, Y.L. Chueh, L.J. Chou, Z.L. Wang, Nano. Micro Small **2**, 116 (2006)
25. S. Brovelli, N. Chiodini, F. Meinardi, A. Lauria, A. Paleari, Appl. Phys. Lett. **89**, 153126 (2006)
26. X. Xiang, X.T. Zu, S. Zhu, L.M. Wang, V. Shutthanandan, P. Nachimuthu, Y. Zhang, J. Phys. D. Appl. Phys. **41**, 5 (2008)
27. Z. Heiba, M. Ahmed, S. Ahmed, J. Alloys Compd. **507**, 253 (2010)
28. E. Soleimani, N. Zamani, Acta Chim. Slov. **64**, 644 (2017)
29. M.K. Ghosh, R.K. Send, P.K. Mahapatra, B.B. Panda, Inorg. Chem. Commun. (2022). https://doi.org/10.1016/J.INOCHE.2022.109670
30. V. Tallapally, D. Damma, S.R. Darmakkolla, Chem. Commun. **55**, 1668 (2019)
31. M.A. Sayeed, H.K. Rouf, J. Mater. Res. Technol. **15**, 3409 (2021)
32. J. Li, C. Chen, J. Li, S. Li, C. Dong, J. Mater. Sci. Mater. Electron. **31**, 16539 (2020)
33. I.S. Yahia, I.M. El Radaf, A.M. Salem, G.B. Sakr, J. Alloys Compd. **776**, 1056 (2019)
34. A. Kole, P. Kumbhakar, Results Phys. **2**, 150 (2012)
35. K. Maniammal, G. Madhu, V. Biju, Phys. E Low-Dimensional Syst. Nanostruct. **85**, 214 (2017)
36. D. Nath, F. Singh, R. Physics, Mater. Chem. Phys. **239**, 122021 (2020)
37. B. Panda, P. Mahapatra, M.K. Ghosh, J. Electron. Mater. **47**, 3657 (2018)
38. S.K. Abdel-Aal, A.S. Abdel-Rahman, J. Cryst. Growth **457**, 282 (2017)
39. S. Abdel-Aal, A. Abdel-Rahman, J. Electron. Mater. **48**, 1686 (2019)
40. N. Chakraborty, S. Das, V. Srihari, D. Mondal, D. Saha, A. Konar, S. Mishra, S. Mondal, Mater. Adv. **2**, 3760 (2021)
41. S.F. Ahmed, S. Khan, P.K. Ghosh, M.K. Mitra, K.K. Chattopadhyay, J Sol-Gel Sci Techn **39**, 241 (2006)
42. X. Li, Y. Wang, W. Liu, G. Jiang, C. Zhu, Mater. Lett. **85**, 25 (2012)
43. A.T. Hassan, E.S. Hassan, O.M. Abdulmunem, J. Mech. Behav. Mater. **30**, 304 (2021)
44. Z. Ansari, S. Ansari, T. Ko, J. Ohl, Sens. Actuat. B Chem. **87**, 105 (2002)
45. C. Ke, W. Zhu, J. Pan, Z. Yang, Curr. Appl. Phys. **11**, S306 (2011)
46. C. Kumar, N.K. Mishra, A. Kumar, M. Bhatt, P. Chaudhary, R. Singh, Appl. Nanosci. **6**, 1059 (2016)
47. W. Brzyska, Pol. J. Chem. **75**, 43 (2001)
48. S.K. Abdel-Aal, A.S. Abdel-Rahman, W.M. Gamal, M. Abdel-Kader, H.S. Ayoub, A.F. El-Sherif, M.F. Kandeel, S. Bozhko, E.E. Yakimov, E.B. Yakimov, Acta Crystallogr. Sect. B Struct. Sci. Cryst. Eng. Mater. **75**, 880 (2019)
49. C.G. Granqvist, Thin Solid Films **194**, 730 (1990)
50. B.S.R. Devi, R. Raveendran, A.V. Vaidyan, Pramana—J. Phys. **68**, 679 (2007)
51. M. Bagheri, M. Saremi, J. Phys. D. Appl. Phys. **37**, 1248 (2004)
52. D. Chen, L. Gao, J. Colloid Interface Sci. **279**, 137 (2004)
53. S.A. Ansari, M.M. Khan, M.O. Ansari, J. Lee, M.H. Cho, New J. Chem. **38**, 2462 (2014)
54. B.B. Panda, B. Sharma, R.K. Rana, Adv. Sci. Eng. Med. **8**, 333 (2016)
55. V. Tallapally, R. Esteves, L. Nahar, I. Arachchige, Chem. Mater. **28**, 5406 (2016)
56. F. Hanini, H. Farh, M. Khechba, A. Bouabellou, S. Gattal, Defect Diffus Forum **397**, 8 (2019)
57. S.K. Tripathy, Opt. Mater. (Amst). **46**, 240 (2015)
58. J. Henry, K. Mohanraj, G. Sivakumar, J. Asian Ceram. Soc. **4**, 81 (2016)

59. N. Huse, A. Dive, K. Gattu, R. Sharma, Mater. Sci. Semicond. Process. **67**, 62 (2017)
60. F. Koohyar, J. Thermodyn. Catal. **4**, 1 (2013)
61. H.S. Bolarinwa, M.U. Onuu, A.Y. Fasasi, S.O. Alayande, L.O. Animasahun, I.O. Abdulsalami, O.G. Fadodun, I.A. Egunjobi, J. Taibah Univ. Sci. **11**, 1245 (2017)
62. R. Singh, R.K. Ulrich, Electrochem. Soc. Interface **8**, 26 (1999)
63. S. Mahato, A.K. Kar, J. Sci. Adv. Mater. Devices **2**, 165 (2017)
64. B. Aly, Phys. Scr. **95**, 065807 (2020)